JOURNAL OF MATERIALS SCIENCE 27 (1992) 4160–4166

Fracture behaviour and microstructure of $MoSi_2$ reinforced with ductile ellipsoidal Nb particles

J. BESSON, M. DE GRAEF, J. P. A. LÖFVANDER, S. M. SPEARING
Materials Department, College of Engineering, University of California, Santa Barbara, CA 93106, USA

A $MoSi_2$/Nb composite with ellipsoidal reinforcements has been produced by uniaxial forging of a sample manufactured by hot isostatic pressing (HIP). The final aspect ratio of the reinforcing Nb particles as a function of strain has been predicted. Reaction products at the interface have been identified by means of energy dispersive X-ray analysis, electron diffraction, high resolution electron microscopy and image simulations. Substantial improvements have been obtained in the fracture toughness compared to the unreinforced matrix and $MoSi_2$ reinforced with identical volume fraction of spherical Nb reinforcements. The increase has been interpreted on the basis of a reduced number of particles that totally debond.

1. Introduction

Composites of intermetallics or ceramic matrices reinforced with ductile metal particles are attractive materials for high temperature structural applications. The matrix provides good oxidation and creep resistance whilst the metal particles increase the low temperature toughness. The molybdenum disilicide ($MoSi_2$)/niobium (Nb) system is one such material considered to have potential applications in the 1250–1650 K temperature range [1]. $MoSi_2$ offers excellent high temperature oxidation resistance due to the formation of silica (SiO_2). Niobium is a moderately ductile metal (uniaxial yield stress σ_0 = 140 MPa, failure strain ε_f = 45%) with a relatively high melting temperature (2742 K).

The principle toughening mechanism in such materials is assumed to be the plastic dissipation in the ductile reinforcements bridging the crack faces. At steady state the increase in toughness, ΔG_c, is given by [2, 3]

$$\Delta G_c = f\sigma_0 R\chi \quad (1)$$

where f is the area fraction of ductile material on the fracture surface, σ_0 is the uniaxial yield stress, R is a representative cross-sectional radius of the reinforcement and χ is a work of rupture function which depends on the debond length at the interface between the matrix and reinforcement, the plastic displacement at ligament failure, U^*, and the work hardening coefficient. The magnitude of χ is evaluated in the non-dimensional stress–strain relationship for a single volume element containing a single reinforcement for a non-hardening material:

$$\chi = \int_0^{U^*/R} \frac{\sigma}{\sigma_0} \mathrm{d}\left(\frac{U}{R}\right) \quad (2)$$

where σ is the stress and U the crack opening.

Lu *et al.* [1] studied the $MoSi_2$/Nb system in which the Nb was present as spherical particles. They observed a five-fold increase in the work of rupture over that of the unreinforced matrix. Experience with other composites has shown that much greater toughening can be obtained using particles with high aspect ratios, preferentially orientated parallel to the principle loading direction, with aligned fibres as a limiting case [4–6]. The benefits of such reinforcement include; increasing the number of particles encountered on a given crack plane, which will increase the number of sites at which crack deflection may occur and, secondly, reducing the number of particles which debond entirely from the matrix and, therefore, do not contribute significantly to the toughness.

In Reference 1 the material was processed by hot isostatically pressing (HIP) together $MoSi_2$ and Nb powders. This yielded a dense matrix and a uniform particle distribution. Given the success of this approach, the most straightforward means to obtain a composite with differing particle aspect ratios is to initially follow this procedure [1], but subsequently hot-work the consolidated material so as to deform the particles into a more effective shape. In this paper we investigate the effect of forging an initially HIPed $MoSi_2$/Nb composite. A similar method has been successfully employed for a TiAl/Nb composite [4]. The microstructure of the forged composite is studied by means of scanning and transmission electron

0022–2461

microscopy (SEM and TEM, respectively). The fine grained microstructure of the reaction zone between the Nb particle and the matrix necessitates the use of medium and high resolution microscopy techniques in order to unambiguously identify the different phases. There are three principle aims of the work which will be addressed in turn:

1. Prediction of the particle aspect ratio, given the hot-working conditions and over-all deformation.
2. Microstructural characterization, with particular emphasis on effects of hot-working which may be detrimental to the composite properties.
3. Measurement of the additional toughening obtained by deforming the niobium particles.

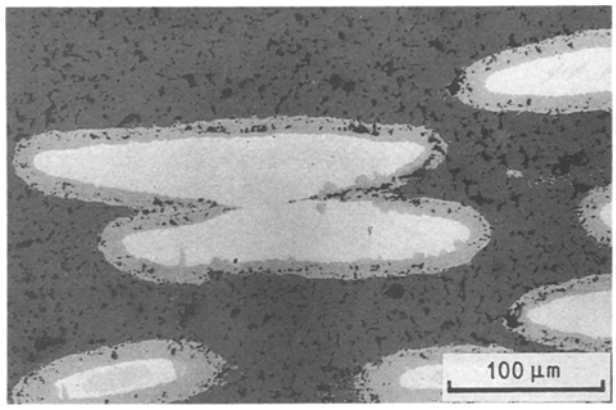

Figure 1 SEM micrograph showing a typical microstructure after HIPing and forging at 1950 K to true deformation, − 0.69.

2. Processing

A high purity $MoSi_2$ powder supplied by Aesar was chosen to produce the matrices (99.9% metallic constituents, particle size 3–10 μm). The $MoSi_2$ powder was blended with 20 volume per cent of spherical niobium powder produced by the plasma rotating electrode process (size 150–212 μm). The mixture was then encapsulated in a Nb can and outgassed for 4 h at 573 K (1.3×10^{-2} Pa). The powder was consolidated in a hot isostatic press (HIP) vessel (ASEA QIH-3) for 2 h at 1623 K under 276 MPa. The initial can dimensions were: diameter 12.5 mm, length 50 mm.

Subsequently the can was mechanically removed and the composite was forged in a vacuum furnace (Vacuum Industries 3600) using graphite pistons at 1950 K under a stress of approximately 25 MPa. Several different amounts of total deformation were obtained in this manner. All microstructures were characterized on a Jeol SM840A scanning electron microscope (SEM) equipped with a Tracor Northern TN5500 energy dispersive spectroscopy (EDS). An example of typical microstructure after processing is shown on Fig. 1, where the ellipsoidal cross-section is evident. The material was also examined with the surface perpendicular to the forging direction and the particle cross-section was determined to be circular.

3. Niobium particle deformation

During forging of the composite, the initially spherical niobium inclusions are deformed into pancake-like particles. This process can be modelled using the Eshelby formalism [7–9]. Both the matrix and the inclusion are assumed to be linear visco-plastic materials (elastic deformation is neglected).

The body is subjected to a remote deformation rate $\tilde{E}^{\infty}$, and it can be shown that the strain rate tensor in the inclusion $\tilde{\varepsilon}$ is uniform and equal to

$$\tilde{\varepsilon} = [\bar{\bar{I}} + \bar{\bar{S}}[\bar{\bar{C}}_m - (\bar{\bar{C}}_m - \bar{\bar{C}}_i)\bar{\bar{S}}]^{-1}(\bar{\bar{C}}_m - \bar{\bar{C}}_i)]\tilde{E}^{\infty} \quad (3)$$

where $\bar{\bar{C}}_i$ and $\bar{\bar{C}}_m$ are, respectively, the stiffness fourth order tensors of the inclusion and the matrix and $\bar{\bar{S}}$ is the Eshelby localization tensor. The previous equation can be easily simplified in the case of forging when both the inclusions and the matrix are isotropic incompressible materials ($\nu = 1/2$). Therefore, the tensors $\bar{\bar{C}}_i$ and $\bar{\bar{C}}_m$ only depend on the shear moduli μ_i and μ_m. The initial inclusions are spheres which are transformed into oblate (forging) or prolate (extrusion) particles due to the axisymmetric (about the Ox_1 axis) loading conditions ($E^{\infty}_{22} = E^{\infty}_{33} = -1/2E^{\infty}_{11}$ and $\varepsilon_{22} = \varepsilon_{33} = -1/2\varepsilon_{11}$); note also that the particles do not rotate. Noting that the particles are symmetric about the Ox_1 axis, Equation 3 can be rewritten as

$$\frac{\varepsilon_{11}}{E_{11}} = \frac{1}{1-(1-\eta)(S_{1111}-S_{1122})} = \Lambda \quad (4)$$

where $\eta = \mu_i/\mu_m$. Note that μ_m represents the shear modulus of an already homogenized matrix surrounding each inclusion which actually consists of the matrix material ($MoSi_2$) and of the inclusions (Nb). $(S_{1111} - S_{1122})$, which depends only on the aspect ratio of the inclusion, can easily be calculated in the case of oblate or prolate spheroids [7]. The aspect ratio r is given by

$$r = e^{-3/2\int \varepsilon_{11} dt} = e^{-3/2\int \Lambda E_{11} dt} \quad (5)$$

Due to the complex expression for $(S_{1111} - S_{1122})$ [7], the integral in Equation 5 is evaluated numerically. The final aspect ratio is plotted in Fig. 2 as a function of the total applied remote deformation $(\int E_{11} dt)$ for different values of η. For a perfectly rigid inclusion ($\eta = \infty$) no deformation occurs; a perfectly soft inclusion ($\eta = 0$) is also significantly more deformed than an inclusion of the same stiffness as the matrix ($\eta = 1$).

Literature data on the creep behaviour of $MoSi_2$ show that the stress exponent decreases with increasing temperature (Fig. 3, [10, 11]), so that it is likely to be equal to 1 at 1950 K (diffusional creep). Low stress exponents are sometimes found at low temperature and are probably due to the presence of a glassy phase (SiO_2) promoting grain boundary sliding. In either case one can consider that the matrix has a linear visco-plastic behaviour; consequently, the Eshelby model can be applied straightforwardly.

Particle dimensions were measured on SEM micrographs for different amounts of deformation. It should be noted that the aspect ratio of any section of an ellipsoid in a plane parallel to the forging axis is equal to the aspect ratio of this ellipsoid. It is likely that at

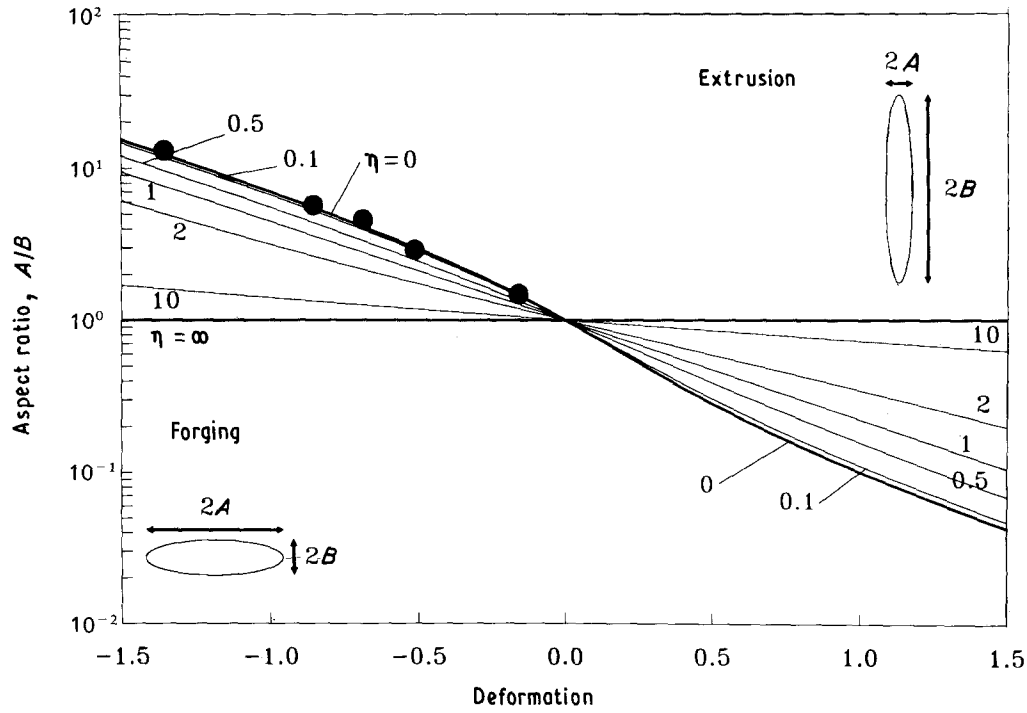

Figure 2 Predicted aspect ratios versus true deformation for initially spherical linear visco-plastic inclusions embedded in a linear matrix. Different curves correspond to different stiffness ratios μ_i/μ_m. The experimental results from this study are superimposed (●).

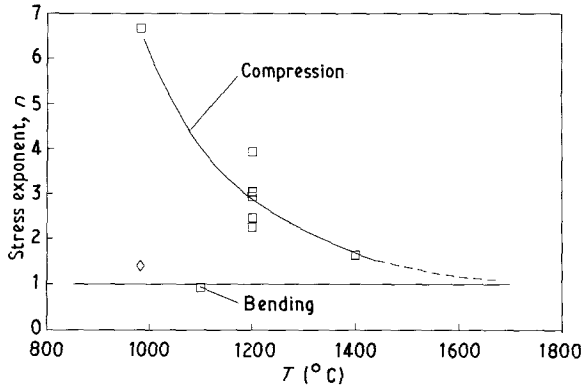

Figure 3 Stress exponent of $MoSi_2$ versus temperature (□ [10], ◇ [11]).

the processing temperature the niobium particles are much softer than the matrix ($\eta \approx 0$). In that case the deformation mechanisms in the niobium particles play no role in the shape change process and Equation 3 can be rewritten as

$$\tilde{\varepsilon} = [\bar{\bar{1}} + \bar{\bar{S}}(\bar{\bar{1}} - \bar{\bar{S}})^{-1}]\tilde{E}^{\infty} \quad (6)$$

or

$$\frac{\varepsilon_{11}}{E_{11}} = \frac{1}{1 - (S_{1111} - S_{1122})}$$

This formula is independent of both $\bar{\bar{C}}_i$ and $\bar{\bar{C}}_m$. The experimental measurements and the theoretical predictions are plotted together in Fig. 2. The comparison of experimental aspect ratios for different deformations with the predictions of Eshelby's model for $\eta \approx 0$ is good.

4. The microstructure

HIPed and forged samples (true deformation −0.69) were cut into 3 mm diameter discs perpendicular to the forging direction and subsequently prepared for transmission electron microscopic (TEM) observations by dimple grinding and ion milling. The samples were characterized using a Jeol 2000FX microscope operated at 200 kV, equipped with a Link eXL energy dispersive high angle X-ray detector and a Jeol 4000FX microscope operated at 400 kV, equipped with a Tracor energy dispersive high angle X-ray detector and a Gatan optical fibre camera system. Computer simulations and indexing of electron diffraction patterns were carried out on an IBM RISC6000/320 with the EMS software package [12].

There are several possible intermetallic phases in the Nb–$MoSi_2$ system; Table I lists the crystallographic data [13] for the phases relevant to this work.

From the Nb–Si binary phase diagram it is deduced that at temperatures below 2056 K Nb is in equilibrium with tetragonal Nb_5Si_3; this contrasts with the presence of the Mo_3Si phase in the Mo–Si system, i.e. there is no corresponding Nb_3Si phase. Notice also that the high temperature forms of Mo_5Si_3 and Nb_5Si_3 (i.e. both the hexagonal and the tetragonal variants) have the same crystal structure and almost identical lattice parameters; consequently a solid solution between the two phases can be expected. However, at low temperature the crystal structures are quite different (although the space groups are the same) and hence a solid solution range is not to be expected.

All the Nb-particles are surrounded by a reaction zone, as can be seen in the SEM micrograph of Fig. 4; the reaction layer is approximately 10–15 μm thick. The chemical composition as determined by EDS at locations A, B, C and D in Fig. 4 are given in Table II. These compositions compare well with EDS results obtained in the TEM. Next to the Nb-particles hexagonal Nb_5Si_3 grains were identified with only trace

TABLE I Crystallographic data for the phases of interest in this work (compound, lattice parameters in nm and space group)

Compound	a	c	Crystal class	Spacegroup
$MoSi_2$	0.3202	0.7851	Tetragonal	$I4/mmm$
Mo_3Si	0.4890	–	Cubic	$Pm3n$
Mo_5Si_3 ($\approx$ 1273 K)	0.9642	0.4910	Tetragonal	$I4/mcm$
Mo_5Si_3 (C-stabilized)	0.7286	0.5002	Hexagonal	$P6_3/mcm$
Nb_5Si_3 (< 1923 K)	0.6570	1.1884	Tetragonal	$I4/mcm$
Nb_5Si_3 (> 1923 K)	1.0026	0.5072	Tetragonal	$I4/mcm$
Nb_5Si_3 (impure)	0.7536	0.5249	Hexagonal	$P6_3/mcm$

TABLE II Compositions in at % as measured by EDS from the regions labelled A–D in Fig. 4

Location	Mo	Si	Nb
A	29.0	71.0	–
B	20.6	43.1	36.3
C	2.1	42.3	55.6
D	–	–	100.00

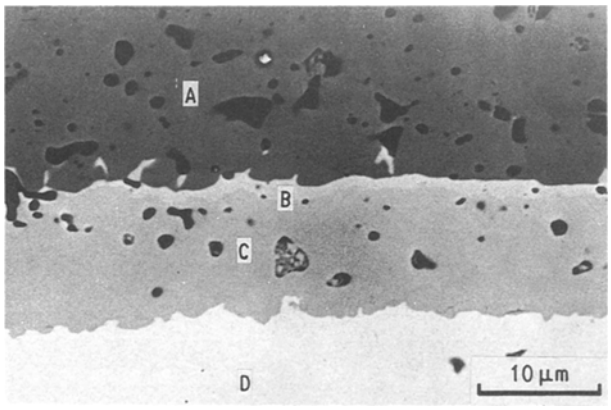

Figure 4 SEM micrograph showing the interface reaction zone between Nb and $MoSi_2$. See Table II for chemical compositions of areas indicated A through D.

amounts of Mo (less than 2 at %). On the outer side of the reaction layer intermixed hexagonal and tetragonal $(Mo,Nb)_5Si_3$ grains were observed; in most tetragonal grains the Mo/Nb ratio was approximately 3. In hexagonal grains this ratio varied from 0.2 to 3.

Evidence for the presence of both hexagonal and tetragonal $(Mo,Nb)_5Si_3$ was obtained through electron diffraction and high resolution imaging. In Fig. 5a the [0 0 0 1] zone axis pattern of the hexagonal $(Mo,Nb)_5Si_3$ is shown; this can be compared to the computed electron diffraction pattern in Fig. 5b (kinematical diffraction approximation), for the ratio Mo/Nb = 3. Fig. 5c shows an experimental high resolution micrograph of a region close to the edge of a hexagonal reaction zone particle; the image contrast changes drastically from the thin edge (at the left) towards the thicker interior of the particle. This image is to be compared to the multi-slice image simulation in Fig. 5d; the simulated image is composed of 25 separate images, corresponding to 0.63 nm thickness increments, starting from a thickness of 3.94 nm at the left. The simulation therefore represents a through-thickness series at defocus 140.0 nm (spherical aberation 3 mm, defocus spread 10 nm and beam convergence angle 0.6 mrad). The inset in Fig. 5c represents the crystal structure, projected along the [0 0 0 1] zone axis. An excellent agreement between the experimental and simulated images can be observed.

The tetragonal particles were also studied by means of high resolution electron microscopy (HREM) techniques; some of the results are shown in Fig. 6. Fig. 6a and b show, respectively, the [0 0 1] structure projection and zone axis pattern; the beams in a circle with radius R were allowed into the objective aperture. Fig. 6c and d show experimental high resolution electron micrographs for two different defocus values; these were digitized and rotationally averaged over 100 unit cells. The resulting enhanced images are shown in Fig. 6e and f. Although no perfect image match was found for this orientation, all experimental images do show the same features and the same symmetry as the projected lattice potential, as is required by standard image formation theory.

The presence of hexagonal Nb_5Si_3 adjacent to the reinforcing Nb particles is to be expected due to interdiffusion of the elements. The phase was listed as contaminated by Pearson [13], however no other elements were detected apart from a small concentration of Mo. The tetragonal forms of Mo_5Si_3 and high temperature Nb_5Si_3, both with $I4/mcm$ spacegroup, have similar lattice parameters (less than 4% difference). The narrow composition range found is somewhat surprising since a complete solid solubility would be expected. It is interesting to note that the high temperature form of Nb_5Si_3 was reported by Lu *et al.* [1] despite their relatively low processing temperature.

The hexagonal form of Mo_5Si_3 was found to exist separately from the hexagonal Nb_5Si_3 with almost identical lattice parameters (difference less than 5%). This phase exhibited a large compositional range of ratios Mo versus Nb. It has been claimed [13] that this phase can only exist when stabilized by carbon. The presence of C in the present samples was not substantiated.

5. Toughness and fractography

The toughness of the composite was measured using chevron notch specimens loaded in three point bending. The specimens were rectangular section beams ($2.2 \times 4.4 \times 23.0\ mm^3$). The loading span was 16 mm. The plane of the ellipsoidal particles was

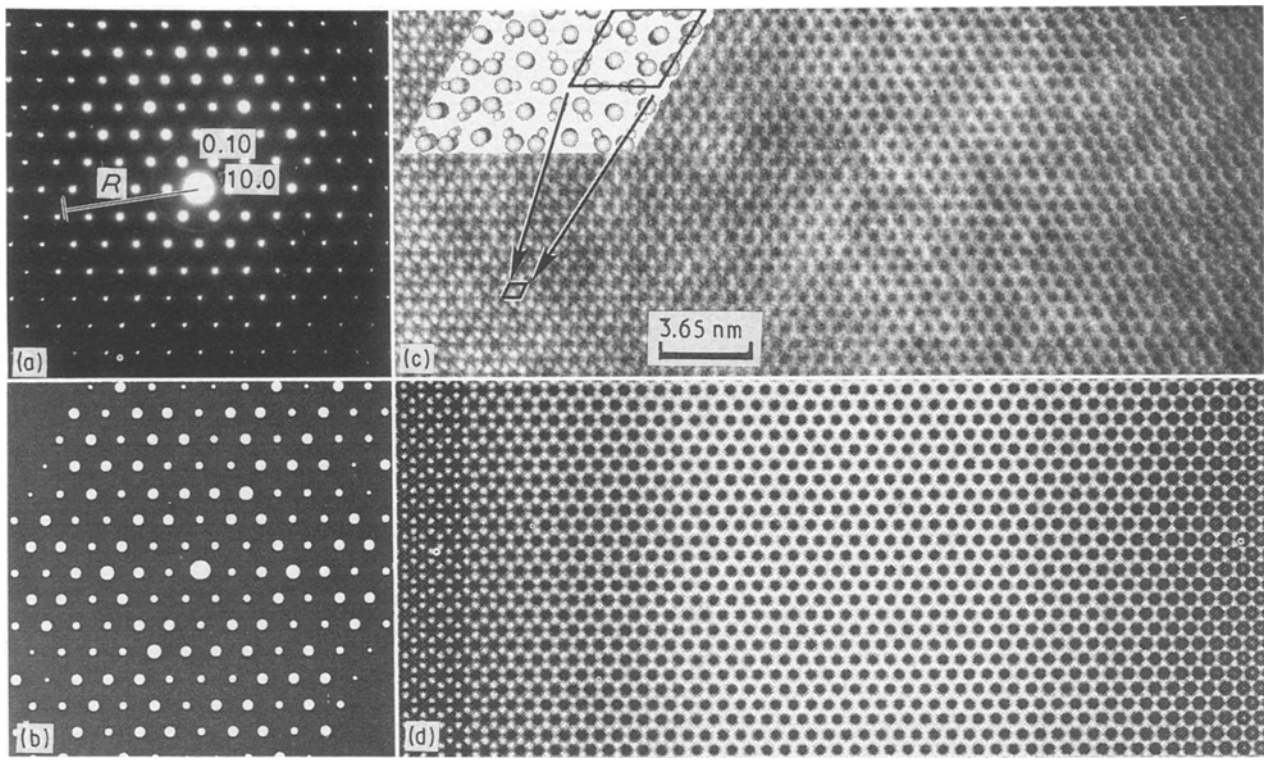

Figure 5 (a) Hexagonal [0 0 0 1] zone axis pattern of a $(Mo,Nb)_5Si_3$ grain for the ratio Mo/Nb = 3; (b) corresponding simulated diffraction pattern (kinematical approximation); (c) experimental high resolution micrograph of a wedge shaped crystal edge (inset shows structure projection); (d) simulated image (through-thickness) series for the parameters stated in the text.

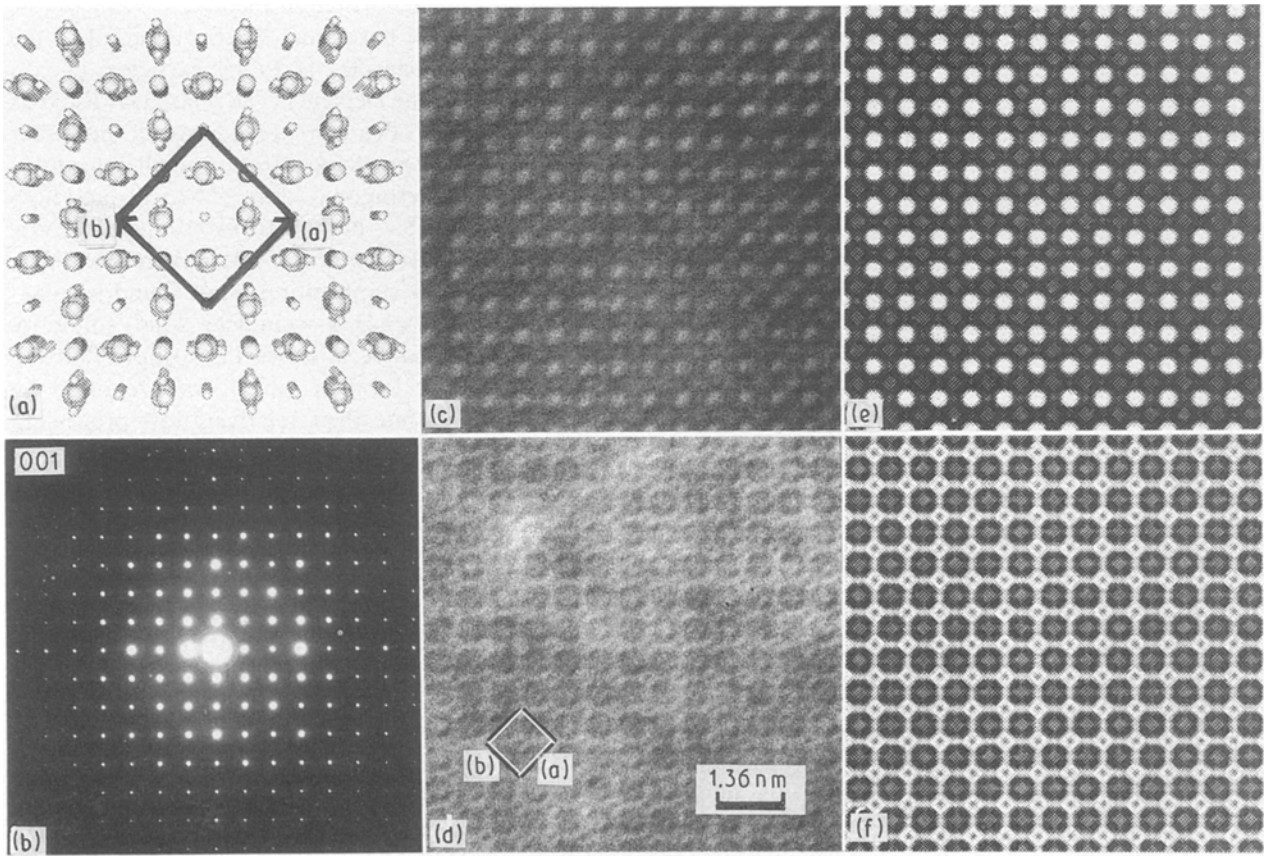

Figure 6 (a) Tetragonal [0 0 1] structure projection; (b) zone axis pattern of a $(Mo,Nb)_5Si_3$ grain for the ratio Mo/Nb = 1; (c) and (d) experimental high resolution micrographs for two different defocus values; (e) and (f) digitized and rotationally averaged images for (c) and (d).

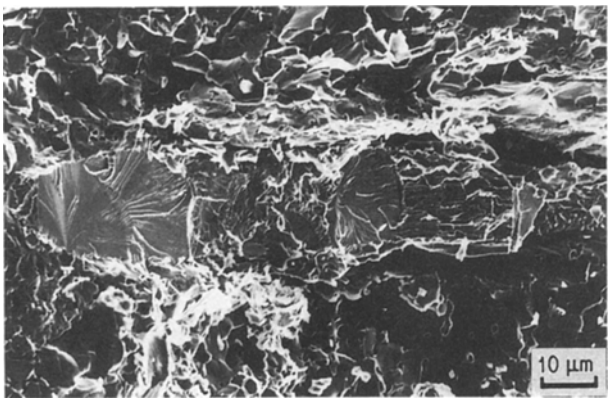

Figure 7 SEM micrograph of a fracture surface showing both brittle and ductile fracture in the Nb particles.

oriented perpendicular to the crack plane and parallel to the depth of the beam. Load versus loading point displacement curves were recorded for each test. The work of rupture, W_R, was calculated by measuring the area under the load displacement curve and dividing by the area of fracture surface. In all cases stable crack growth occurred. For the forged $MoSi_2$/Nb, $W_R = 465\ J\,m^{-2}$. This value compares very favourably with those reported for spherical reinforcing particles ($W_R = 264\ J\,m^{-2}$ [1]) and the unreinforced matrix ($W_R = 57$–$75\ J\,m^{-2}$ [1, 14, 15]) – W_R is calculated from the toughness data using the formula

$$W_R = \frac{1}{1-\nu^2}\frac{K_{IC}^2}{E}$$

the Young's modulus, E, being equal to 400 GPa and the Poisson ratio, ν, to 0.25.

The fracture surface was macroscopically rough, indicating considerable crack deflection. Some of the niobium particles had debonded without fracturing, in general, they were intersected by the crack near their edges. Most particles failed by ductile rupture or cleavage with no significant debonding. In the absence of debonding the plastic stretch was small, typically 15% of the particle thickness on each fracture surface (i.e. $U^* = 0.6R$ in total). It is not understood why cleavage should occur in preference to ductility in an unexpectedly high proportion of particles; similar observations were made by Lu *et al.* [1], which suggests that the forging process does not significantly alter the ductility of the niobium.

It is possible to make an estimate of the available increase in toughening using Equation 1. A linear strain softening relationship is a reasonable lower bound on the true tensile stress-stretch behaviour.

$$\frac{\sigma}{\sigma_0} = \left(\frac{\sigma}{\sigma_0}\right)_{U^*=0}\left[1 - \frac{U}{U^*}\right] \qquad (7)$$

For the non-debonding case [16] $(\sigma/\sigma_0)_{U=0} = 4.5$ and from the fracture observations ($U^*/R = 0.6$); thus $\chi = 1.35$. Assuming the fraction of Nb that fails by ductile rupture is approximately 0.5 (probably an overestimate), and the over-all volume fraction of Nb is 0.2, hence $f = 0.1$. The flow stress of Nb is 140 MPa, thus: $\Delta G = 380\ J\,m^{-2}$. Given a matrix toughness of $65\ J\,m^{-2}$, the expected work of rupture is $445\ J\,m^{-2}$. That the work of rupture measured by Lu *et al.* [1] falls far short of this figure probably indicates that a higher proportion of the particles debonded completely and were, therefore, unable to contribute to the toughening. The observed crack deflection also acts to improve the fracture resistance.

Increased toughness could be obtained if the $MoSi_2$ interface were tailored to allow a controlled amount of debonding. Similarly it would be beneficial to suppress the cleavage failure of the Nb.

6. Summary

It has been shown that it is possible to produce an $MoSi_2$ based composite with aligned ellipsoidal Nb reinforcements by uniaxial forging. The shape of the initially spherical particles is dependent on the amount of total deformation. The final aspect ratios have been accurately predicted by assuming that the Nb inclusions are much softer than the matrix. A reaction layer approximately 10–15 μm thick formed during processing due to the interdiffusion of elements at the particle/matrix interface. Almost pure hexagonal Nb_5Si_3 was observed next to the Nb particles. Intermixed hexagonal and tetragonal $(Mo,Nb)_5Si_3$ grains were present in the outer reaction layer next to the matrix. Stable crack growth occurred during toughness measurements. The work of rupture, W_R, for ellipsoidal reinforcements exhibited a 70% improvement over $MoSi_2$ reinforced with spherical particles and a seven-fold increase over unreinforced $MoSi_2$. Fracture surfaces showed both ductile and cleavage features; little debonding was observed at the particle/matrix interfaces. Further improvements of fracture properties might be obtained by controlling the interface reactions to obtain a controlled amount of debonding.

Acknowledgements

The authors would like to thank Drs T. C. Lu, C. H. Weber and H. Deve for stimulating discussions. M. De Graef is a Research Associate with the Belgian National Science Foundation (NFWO). This work was sponsored by the Defense Advanced Research Projects Agency under a University Research Initiative Grant No. 0014-86-K-0753, supervised by Dr W. W. Barker and monitored by Dr S. G. Fishman of the Office of Naval Research.

References

1. T. C. LU, A. G. EVANS, R. J. HECHT and R. MEHRABIAN, *Acta Metall. Mater.* **39** (1991) 1853.
2. B. BUDIANSKY, J. C. AMAZIGO and A. G. EVANS, *J. Mech. Phys. Solids* **36** (1988) 167.
3. A. G. EVANS and R. M. McMEEKING, *Acta Metall.* **34** (1986) 2435.
4. C. K. ELLIOTT, G. R. ODETTE, G. E. LUCAS and J. W. SHECKHERD, *MRS Proceedings* **120** (1988) 95.
5. M. BANNISTER, PhD Thesis, Cambridge University (1990).
6. M. F. ASHBY, F. J. BLUNT and M. BANNISTER, *Acta Metall.* **37** (1989) 1847.

7. J. D. ESHELBY, *Proc. R. Soc. London* **A241** (1957) 376.
8. B. A. BILBY, J. D. ESHELBY and A. K. KUNDU, *Tectonophysics* **28** (1975) 265.
9. P. GILORMINI and F. MONTHEILLET, *J. Mech. Phys. Solids* **34** (1986) 97.
10. C. H. WEBER, Private communication.
11. Refractory Molybdenum Silicides, Climax Molybdenum Company (1963).
12. P. A. STADELMAN, *Ultramicroscopy* **21** (1987) 131.
13. "Pearson's Handbook of Crystallographic Data for Intermetallic Phases", edited by P. Villars and L. D. Calvert (American Society for Metals, 1985).
14. J. M. YANG, K. KAI and S. M. JENG, *Scripta Metall.* **123** (1989) 1953.
15. F. D. GAC and J. J. PETROVIC, *J. Amer. Ceram. Soc.* **88** (1985) C200.
16. P. W. BRIDGEMAN, in "Studies in Large Plastic Flow and Fracture" (Harvard University Press, 1964).

Received 8 April
and accepted 30 July 1991